

Fractional antiferromagnetic skyrmion lattice induced by anisotropic couplings

<https://doi.org/10.1038/s41586-020-2716-8>

Received: 6 November 2019

Accepted: 15 July 2020

Published online: 23 September 2020

 Check for updates

Shang Gao^{1,2,3,17,18}, H. Diego Rosales^{4,5,6}, Flavia A. Gómez Albarracín^{4,5,6}, Vladimir Tsurkan^{7,8}, Guratinder Kaur^{1,2}, Tom Fennell¹, Paul Steffens⁹, Martin Boehm⁹, Petr Čermák^{10,11}, Astrid Schneidewind¹⁰, Eric Ressouche¹², Daniel C. Cabra^{4,5,13}, Christian Rüegg^{2,14,15,16} & Oksana Zaharko¹✉

Magnetic skyrmions are topological solitons with a nanoscale winding spin texture that hold promise for spintronics applications^{1–4}. Skyrmions have so far been observed in a variety of magnets that exhibit nearly parallel alignment for neighbouring spins, but theoretically skyrmions with anti-parallel neighbouring spins are also possible. Such antiferromagnetic skyrmions may allow more flexible control than conventional ferromagnetic skyrmions^{5–10}. Here, by combining neutron scattering measurements and Monte Carlo simulations, we show that a fractional antiferromagnetic skyrmion lattice is stabilized in MnSc₂S₄ through anisotropic couplings. The observed lattice is composed of three antiferromagnetically coupled sublattices, and each sublattice is a triangular skyrmion lattice that is fractionalized into two parts with an incipient meron (half-skyrmion) character^{11,12}. Our work demonstrates that the theoretically proposed antiferromagnetic skyrmions can be stabilized in real materials and represents an important step towards their implementation in spintronic devices.

The concept of topology has revolutionized condensed matter physics: it reveals that the classification of different phases can extend beyond the Landau–Ginzburg–Wilson paradigm of classification by symmetry, generating a variety of new phases with topological characters¹³. Among topological entities, magnetic skyrmions with a winding spin texture in real space have triggered enormous interest owing to their potential for spintronics applications^{1–4}. Information encoded in the nanoscale spin winding of the skyrmions is topologically protected against perturbations, and can be conveniently manipulated with electronic currents^{14–16}.

Similar to the vortices that emerge in the Berezinskii–Kosterlitz–Thouless transition, magnetic skyrmions are conventionally treated as topological solitons in nonlinear field theory¹⁷, which implies a continuous ferromagnetic spin alignment at short length scales. This short-range ferromagnetism is indeed a common feature for most of the known skyrmion hosts, including chiral magnets with antisymmetric Dzyaloshinskii–Moriya interactions³ and the recently discovered centrosymmetric compounds with multiple spin couplings^{18–20}.

However, explorations on skyrmions should not be confined to ferromagnets²¹. Theoretical calculations have suggested that skyrmions might be also stabilized in antiferromagnets with two^{6,7} or three^{8–10} sublattices, leading to antiferromagnetic skyrmions with anti-parallel nearest-neighbour spin alignment, which might complement skyrmion

control in spintronic devices⁵. On the other hand, antiferromagnets are often accompanied by strong frustration, which is known to enhance fluctuations²². Thus, the marriage between skyrmion and antiferromagnetism^{23,24} might be key to realizing exotic states such as magnetic hopfions^{25,26} or even quantum skyrmions²⁷.

Despite their exciting prospects, it is still unclear whether antiferromagnetic skyrmions can be experimentally realized or not. Direct observation of antiferromagnetic skyrmions, for example, with Lorentz transmission electron microscopy², is challenging because the alternating spins cancel the local magnetic field. Although magnetic structures described by a single propagation vector \mathbf{q} can be accurately determined by neutron diffraction, skyrmion lattices are multi- \mathbf{q} structures and the phase factors between the different propagation vectors \mathbf{q} are lost. One prominent example is the spinel MnSc₂S₄ (refs. 28,29), where the magnetic Mn²⁺ ions form a bipartite diamond lattice (see Fig. 1a). A previous neutron diffraction work revealed the existence of a field-induced triple- \mathbf{q} phase in this antiferromagnet²⁹, but the exact arrangement of magnetic moments remains unclear.

Here, we show that a fractional three-sublattice antiferromagnetic skyrmion lattice is realized in the MnSc₂S₄ triple- \mathbf{q} phase. By combining state-of-the-art neutron spectroscopy, extensive Monte Carlo simulations and neutron diffraction, we clarify the microscopic couplings between the Mn²⁺ spins in MnSc₂S₄ up to the third-neighbours and, most

¹Laboratory for Neutron Scattering and Imaging, Paul Scherrer Institut, Villigen, Switzerland. ²Department of Quantum Matter Physics, University of Geneva, Geneva, Switzerland. ³RIKEN Center for Emergent Matter Science, Wako, Japan. ⁴Instituto de Física de Líquidos y Sistemas Biológicos (IFLYSIB), UNLP-CONICET, Facultad de Ciencias Exactas, La Plata, Argentina. ⁵Departamento de Física, Facultad de Ciencias Exactas, Universidad Nacional de La Plata, La Plata, Argentina. ⁶Departamento de Ciencias Básicas, Facultad de Ingeniería, Universidad Nacional de La Plata, La Plata, Argentina. ⁷Experimental Physics V, University of Augsburg, Augsburg, Germany. ⁸Institute of Applied Physics, Chisinau, Republic of Moldova. ⁹Institut Laue-Langevin, Grenoble, France. ¹⁰Jülich Center for Neutron Science, Heinz Maier-Leibnitz Zentrum, Forschungszentrum Jülich GmbH, Garching, Germany. ¹¹Department of Condensed Matter Physics, Faculty of Mathematics and Physics, Charles University, Prague, Czech Republic. ¹²Université Grenoble Alpes, CEA, INAC-MEM, Grenoble, France. ¹³Abdus Salam International Centre for Theoretical Physics, Associate Scheme, Trieste, Italy. ¹⁴Neutrons and Muons Research Division, Paul Scherrer Institut, Villigen, Switzerland. ¹⁵Institute for Quantum Electronics, ETH Zürich, Zurich, Switzerland. ¹⁶Institute of Physics, École Polytechnique Fédérale de Lausanne, Lausanne, Switzerland. ¹⁷Materials Science and Technology Division, Oak Ridge National Laboratory, Oak Ridge, TN, USA. ¹⁸Neutron Science Division, Oak Ridge National Laboratory, Oak Ridge, TN, USA. ✉e-mail: oksana.zaharko@psi.ch

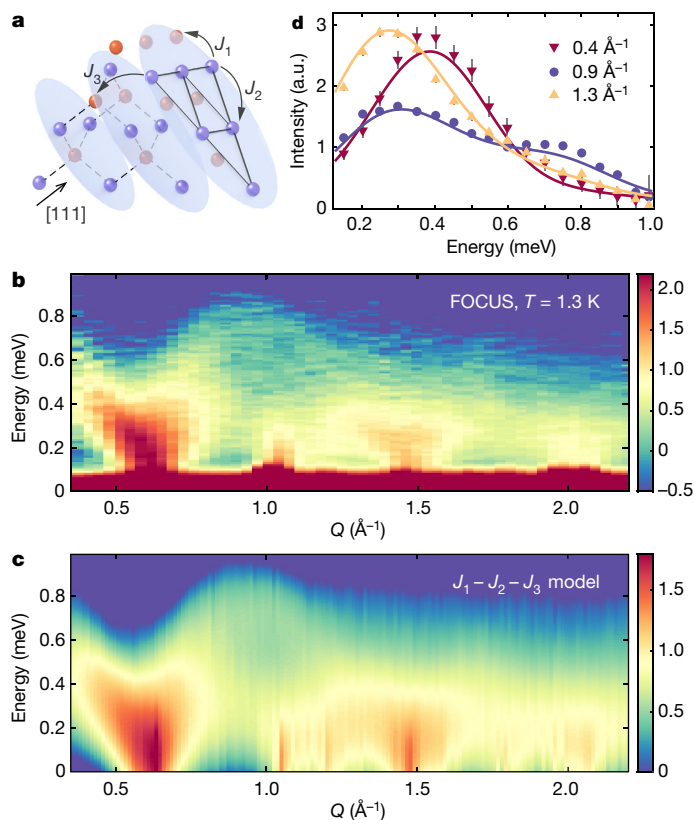


Fig. 1 | Spin dynamics in a powder sample of MnSc_2S_4 . **a**, Mn^{2+} ions (blue and brown spheres) in MnSc_2S_4 form a bipartite diamond lattice that can be viewed as triangular planes (blue) stacked along the [111] direction. Couplings up to the third neighbours are indicated. Information on the magnetic lattice in the cubic unit cell can be found in ref. ²⁹. **b**, INS spectra $S(Q, \omega)$ as a function of wavevector Q and energy transfer $\hbar\omega$ (\hbar , reduced Planck constant) collected on FOCUS at $T = 1.3$ K using a powder sample of MnSc_2S_4 (see Methods). **c**, INS spectra calculated using the linear spin-wave theory for the J_1 - J_2 - J_3 model with $J_1 = -0.31(1)$ K, $J_2 = 0.46(1)$ K and $J_3 = 0.087(4)$ K. The calculated spectra are convoluted by a Gaussian function with a fitted full-width at half-maximum (FWHM) of 0.27 meV to account for the instrumental resolution and thermal broadening. **d**, Integrated INS spectra $I(\omega)$ at $Q = 0.4 \text{ \AA}^{-1}$ (red triangles), 0.9 \AA^{-1} (blue circles) and 1.3 \AA^{-1} (yellow triangles) with an integration width of 0.1 \AA^{-1} . Solid lines are the fitted spectra using the J_1 - J_2 - J_3 model at the corresponding Q positions. Error bars represent standard deviations. a.u., arbitrary units.

importantly, establish the existence of a fractional three-sublattice antiferromagnetic skyrmion lattice^{8–10} that originates from anisotropic couplings between nearest neighbours. The fractionalization of the antiferromagnetic skyrmions can be attributed to their close packing¹¹, which leads to incomplete spin wrapping that is reminiscent of magnetic merons/antimerons¹².

Inelastic neutron scattering (INS) probes the magnon excitations in long-range ordered magnets. Compared to neutron diffuse scattering, which was used to characterize the quasi-elastic spiral spin-liquid correlations in the same compound²⁹, the rich information that is available in INS spectra allows the direct study of further neighbour couplings in the spin Hamiltonian, which are crucial for understanding the phase transitions in MnSc_2S_4 ^{30–32}.

Figure 1b shows our inelastic neutron spectra, collected on a powder sample of MnSc_2S_4 at temperature $T = 1.3$ K in the helical ordered state, which is the parent phase of the field-induced triple- \mathbf{q} state²⁹. Strong INS intensities are observed, emanating from the magnetic Bragg reflections that correspond to the propagation vector $\mathbf{q} = (0.75, 0.75, 0)$ and reaching a maximal energy of $E \approx 0.9$ meV at wavevector $Q \approx 0.9 \text{ \AA}^{-1}$. Compared to other similar spinel compounds^{33–35}, the

magnon dispersion bandwidth in MnSc_2S_4 is narrower, consistent with its relatively low ordering temperature of $T_N = 2.3$ K (refs. ^{28,29}).

Figure 2 presents our INS results, collected on a single-crystal sample of MnSc_2S_4 along the high-symmetry lines $(h, h, 0)$, $(h, 1.5 - h, 0)$ and $(h, 0.75, 0)$ in reciprocal space. No excitation gap can be resolved, which is compatible with the absence of single-ion anisotropy up to the second order in spin operators owing to the $3d^5$ electron configuration of the Mn^{2+} ions³⁶. A representative energy scan at $(0, 0.75, 0)$ shown in Fig. 2a reveals broad excitations, suggesting the appearance of multiple magnon bands.

Using linear spin-wave theory, we are able to model the spin dynamics with the Hamiltonian $\mathcal{H}_0 = \sum_{ij} J_{ij} \mathbf{S}_i \cdot \mathbf{S}_j$, where J_{ij} is the exchange coupling between the Heisenberg spins \mathbf{S}_i and \mathbf{S}_j . As explained in Methods and shown in Extended Data Fig. 1, it is necessary to include couplings up to the third neighbours^{30–32} to reproduce the measured INS spectra. The fitted coupling strengths are $J_1 = -0.31(1)$ K, $J_2 = 0.46(1)$ K, and $J_3 = 0.087(4)$ K at the nearest, second and third neighbours, respectively. The uncertainties are standard errors from least-squares fits. Representative fits to the powder data at selected Q positions are shown in Fig. 1d. The overall calculated spectra are presented in Fig. 1c and Fig. 2e, f for comparison with the powder and single-crystal experimental data, respectively. As shown in Fig. 2a for the energy scan at $(0, 0.75, 0)$, contributions from different magnetic domains are necessary to describe the broad excitations in the single-crystal data.

Although the J_1 - J_2 - J_3 model successfully captures the spin dynamics in the helical phase of MnSc_2S_4 , it fails to account for the field-induced triple- \mathbf{q} phase²⁹, which implies the necessity of even weaker perturbations that are beyond the INS resolution. Such a perturbation-dominated scenario is allowed in MnSc_2S_4 owing to its enormous ground-state degeneracy^{29,30}. Theoretical calculations on centrosymmetric systems have revealed that perturbations from the high-order analogues of the Ruderman–Kittel–Kasuya–Yosida (RKKY) interactions can often stabilize a triple- \mathbf{q} phase^{37,38}. However, this mechanism fails in MnSc_2S_4 because the insulating character of this compound rules out any RKKY-like interactions that rely on conduction electrons.

Through extensive Monte Carlo simulations, we explored the effect of different perturbations that are compatible with the symmetries of the lattice³¹, and revealed that the triple- \mathbf{q} phase in MnSc_2S_4 can be stabilized by anisotropic couplings at the nearest neighbours, together with a fourth-order single-ion anisotropy term that might be microscopically derived from spin–orbit coupling and dipolar interactions³¹. The perturbed J_1 - J_2 - J_3 Hamiltonian now reads

$$\begin{aligned} \mathcal{H} = & \mathcal{H}_0 + \mathcal{H}_{\parallel} + \mathcal{H}_A + \mathcal{H}_{\text{Zeeman}} \\ = & \sum_{ij} J_{ij} \mathbf{S}_i \cdot \mathbf{S}_j + 3J_{\parallel} \sum_{ij \in \text{NN}} (\mathbf{S}_i \cdot \hat{\mathbf{r}}_{ij})(\mathbf{S}_j \cdot \hat{\mathbf{r}}_{ij}) \\ & + A_4 \sum_{i, \alpha=x,y,z} (S_i^{\alpha})^4 - g\mu_B \mathbf{B}_{\text{III}} \sum_i \mathbf{S}_i, \end{aligned} \quad (1)$$

where \mathcal{H}_{\parallel} is the perturbation term corresponding to nearest-neighbour anisotropic couplings, J_{\parallel} is the anisotropic coupling strength and $\hat{\mathbf{r}}_{ij}$ is the unitary direction vector along the nearest-neighbour bonds; \mathcal{H}_A describes a weak fourth-order single-ion anisotropy that is needed to stabilize a zero-field helical ground state³⁶; $\mathcal{H}_{\text{Zeeman}}$ is the conventional Zeeman term for spins in a magnetic field \mathbf{B}_{III} along the [111] direction; and g and μ_B are the Landé g -factor and the Bohr magneton, respectively. In our minimal Hamiltonian, the anisotropic J_{\parallel} is found to be the only term that can induce a triple- \mathbf{q} phase. Through comparison with the experimental phase diagram presented in Fig. 3, the perturbation parameters can be determined to be $J_{\parallel} = -0.01$ K and $A_4 = 0.0016$ K. As exemplified in Fig. 3a, only one triple- \mathbf{q} domain with propagation vectors lying within the (111) plane is stabilized in field²⁹, and the consequent non-monotonous evolution of the domain distribution is successfully reproduced in our simulations. As presented in Methods

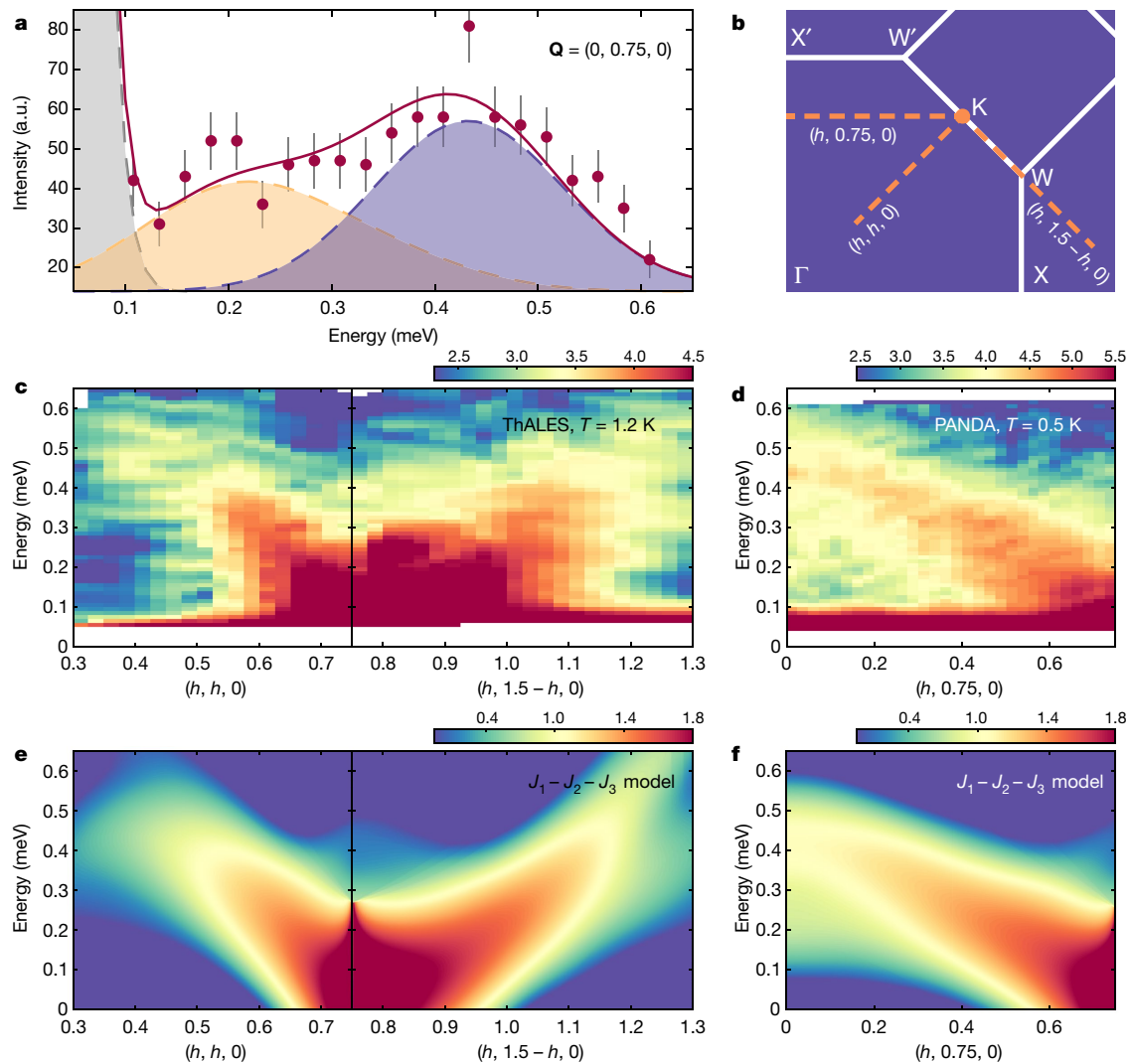


Fig. 2 | Spin dynamics in a single-crystal sample of MnSc_2S_4 . **a**, Representative INS spectra $I(\omega)$ (red circles) collected on PANDA at $T = 0.5$ K and $\mathbf{Q} = (0, 0.75, 0)$ (see Methods). The red solid line denotes the spectra calculated using the J_1 - J_2 - J_3 model. Dashed lines with shaded areas indicate the contributions of magnon scattering from the $(0.75, \pm 0.75, 0)$ and $(0, 0.75, \pm 0.75)$ magnetic domains (yellow), magnon scattering from the $(0.75, 0, \pm 0.75)$ magnetic domains (blue) and the tail of the elastic line (grey). The calculated spectra are convoluted by a

Gaussian function with a fitted FWHM of 0.21 meV to account for the instrumental resolution and thermal broadening. Error bars represent standard deviations. **b**, Brillouin zone in the $(hk0)$ plane with conventional notations. INS spectra are measured along the yellow dashed lines. **c**, INS spectra measured on ThALES at $T = 1.2$ K along the $(h, h, 0)$ and $(h, 1.5 - h, 0)$ directions (see Methods). **d**, INS spectra measured on PANDA at $T = 0.5$ K along the $(h, 0.75, 0)$ direction. **e, f**, INS spectra calculated using the J_1 - J_2 - J_3 model.

and shown in Extended Data Fig. 3, the magnitude of the total scalar spin chirality increases sharply upon entering the triple- \mathbf{q} phase, evidencing a magnetic structure that is topologically different from the single- \mathbf{q} helical phase^{8,23}.

Using Monte Carlo simulations, we can directly inspect the triple- \mathbf{q} structure by layers, in which the Mn^{2+} ions form a triangular lattice (see Figs. 1a, 4a). As expected for antiferromagnets, the spin configuration in one layer shown in Fig. 4b involves nearly anti-parallel spins at the nearest neighbours. However, if the whole triangular lattice is separated into three sublattices^{8,10}, as shown in the insets of Fig. 4b, a smooth whirling texture will emerge in each sublattice, and the only difference among the sublattices is an overall shift of whorls. As described in Fig. 4c, d, spins at the centres of the whorls are anti-aligned with the field, leading to a texture that is similar to that of skyrmion lattices¹. Owing to the short distance between the centres of the whorls, skyrmions in the triangular sublattices are not wrapping the full sphere, but are fractionalized into two blocks with opposite winding directions¹¹, forming a pair of an incipient meron and an antimeron¹², as indicated in Fig. 4d. When the three sublattices are added together as shown schematically

in Fig. 4b, fractional skyrmions with opposite magnetizations overlap in the whole triangular lattice, leading to oscillating S_{III} components near the centre of the whorls and almost- 120° alignments for the S_{\perp} components close to the periphery, where S_{III} (S_{\perp}) are magnetic moments along (perpendicular to) the [111] direction. Therefore, each (111) layer in the triple- \mathbf{q} phase realizes a fractional antiferromagnetic skyrmion lattice that is composed of three sublattices⁸.

Stacking of antiferromagnetic skyrmion lattices along the [111] direction is determined by the propagation vectors and the Mn^{2+} positions within the (111) layers. In Methods, we present an analytical ansatz for spins at general positions constructed as a superposition of three helical modulations, and the correctness of the fractional antiferromagnetic skyrmion lattice is verified through comparison against the neutron diffraction dataset shown in Extended Data Fig. 7. The bipartite character of the diamond lattice leads to bilayers with exactly the same spin configurations, as explained in Fig. 4a, thus realizing three consecutive antiferromagnetic skyrmion bilayers with shifted whorl centres. Such a stacking order leads to antiferromagnetic skyrmion tubes along the [111] direction, shown in Fig. 4c, which is a typical feature for many skyrmion lattices^{39,40}.

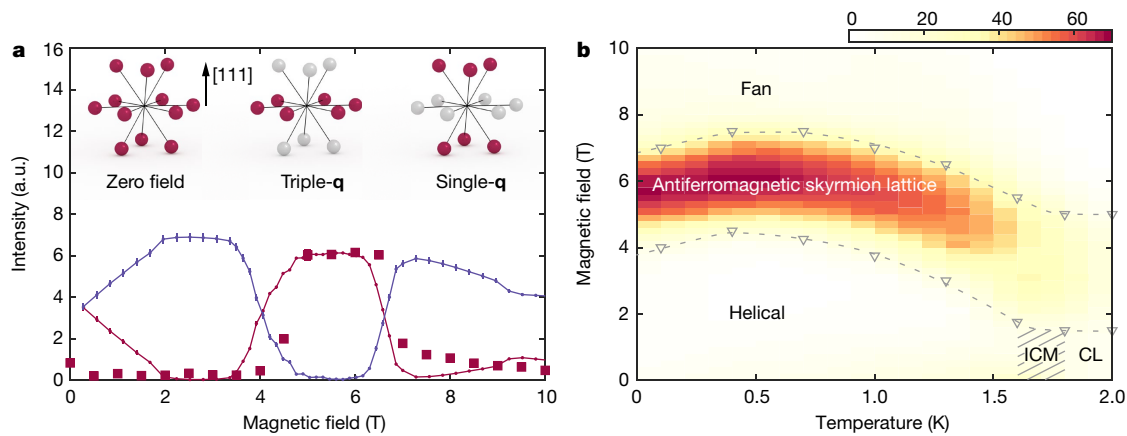


Fig. 3 | Anisotropic-coupling-induced triple-q phase in MnSc_2S_4 . **a**, Evolution of magnetic domains as a function of magnetic field applied along the [111] direction at $T = 0.1\text{ K}$. Red squares are neutron diffraction intensities of the $(0.75, -0.75, 0)$ reflection within the (111) plane measured in a decreasing field. Solid lines are intensities obtained from Monte Carlo simulations, with the averaged contributions from the six arms perpendicular (non-perpendicular) to the [111] direction shown in red (blue). Error bars indicate the standard deviations of the mean. In the intermediate phase region between 3.5 T and 7 T, the six arms perpendicular to the [111] direction have equal intensities, consistent with the triple-q character of MnSc_2S_4 in this region. Insets show the intensity distribution of the $(0.75, 0.75, 0)$ star in the single-q helical phase observed in zero-field cooling (left), the triple-q phase in

an intermediate field (middle) and the single-q helical phase with field-induced domain redistribution (right). Each dot represents a propagation vector, with red (grey) colour indicating non-zero (zero) intensity. **b**, Phase diagram for MnSc_2S_4 obtained from a neutron diffraction experiment performed in a magnetic field along the [111] direction. The colour map shows the intensity of the $(0.75, -0.75, 0)$ reflection collected in a decreasing field, and the phase boundary of the antiferromagnetic skyrmion lattice state is marked by triangles connected by dashed lines as guides to the eye. CL (ICM) stands for the single-q collinear (incommensurate) phase. The Fan phase identified by Monte Carlo simulations is a single-q collinear phase added with a uniform magnetization along the [111] direction. Error bars representing the standard deviations are smaller than the marker size.

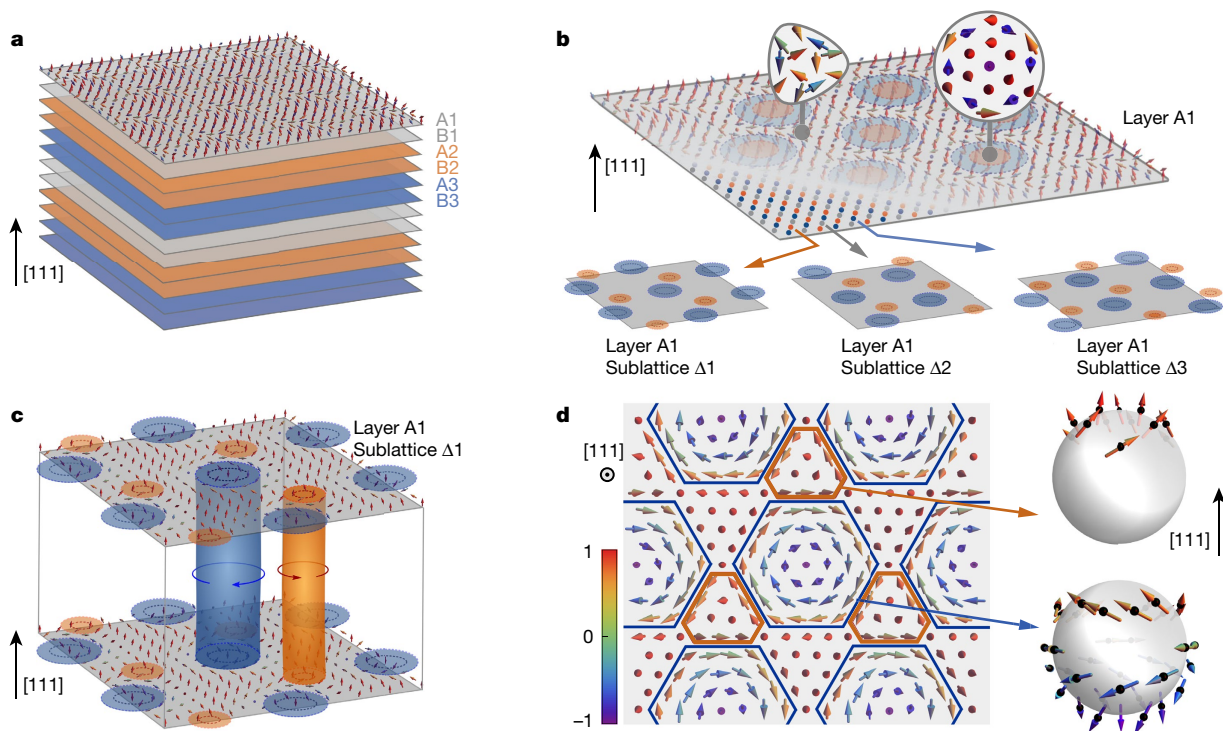


Fig. 4 | Fractional antiferromagnetic skyrmion lattice in MnSc_2S_4 . **a**, Stacking order for the Mn^{2+} triangular lattice layers along the [111] direction. A and B denote the two face-centred cubic sublattices of the diamond lattice shifted by $(1/4, 1/4, 1/4)$, and the Mn^{2+} positions are the same in neighbouring layers of the same colour. Within the A or B sublattice, the triangular lattices in consecutive layers are shifted by $(1/2, 1/2, 0)$, leading to three different types of layer, shown by different colours. **b**, In each layer, the Mn^{2+} triangular lattice can be divided into three sublattices, Δ_1 , Δ_2 and Δ_3 , as illustrated in the insets. In the triple-q phase, Mn^{2+} spins within each triangular sublattice form a fractional skyrmion lattice (see **d**), which leads to a fractional antiferromagnetic skyrmion lattice of three sublattices in the whole layer. Blue and yellow circles

in the insets describe the locations of the fractional skyrmions with opposite winding direction, which overlap with each other in the complete (111) layer. The circular (triangular) inset is a zoomed-in plot of the magnetic structure around the skyrmion centre (boundary). **c**, Spin configurations in the same layer type are exactly the same, leading to cylinders of fractional skyrmions along the [111] direction. **d**, Spin texture of the triangular sublattice Δ_1 in layer A1. The directions of the spins are indicated by arrows, with colours denoting the size of the spin component along the [111] direction. Fractional skyrmions with opposite winding directions are indicated by blue and yellow lines in the main figure, and the wrapping of their spin texture is described in the two spheres shown on the right.

The fractional antiferromagnetic skyrmion lattice established here demonstrates that even antiferromagnets can exhibit topologically non-trivial spin textures. In MnSc_2S_4 , the antiferromagnetic skyrmion lattice inherits the three-sublattice character of the triangular lattice in the (111) layers. However, the mechanism that we discovered, which utilizes anisotropic couplings to stabilize a triple- \mathbf{q} phase, can be generalized to antiferromagnetic systems with different geometries^{41,42}. Especially on the bipartite honeycomb lattice⁴³, anisotropic couplings might stabilize a two-sublattice antiferromagnetic skyrmion lattice with opposite winding spin textures, thus lending an ideal platform to explore antiferromagnetic skyrmion transport^{6,7}.

The spin dynamics of the antiferromagnetic skyrmions also deserves further investigations. In chiral systems, the lifetime of isolated antiferromagnetic skyrmions is known to be enhanced by the Dzyaloshinskii–Moriya interaction⁴⁴. It is therefore interesting to compare the effect of the antisymmetric couplings on the lifetime of antiferromagnetic skyrmions in centrosymmetric systems. For the antiferromagnetic skyrmion lattice, magnons propagating through a topological spin texture might carry a Berry phase and thus experience a fictitious magnetic field^{45,46}, leading to the thermal Hall effect, which can be used for magnonics applications. Furthermore, recent calculations on a three-sublattice antiferromagnetic skyrmion lattice that is similar to the triple- \mathbf{q} phase in MnSc_2S_4 revealed the lowest magnon band to be topologically non-trivial⁹. The consequent chiral magnon edge states allow magnon transport without backscattering⁴⁷ and could further reduce the energy dissipation in magnonics devices.

In summary, our combined neutron scattering and Monte Carlo simulation studies clarify the microscopic spin couplings in MnSc_2S_4 and establish the existence of a fractional antiferromagnetic skyrmion lattice that is induced by anisotropic couplings. Our work shows that topological structures can be stabilized in antiferromagnets, which is an important step in realizing minimal-size spintronic devices with efficient operation.

Online content

Any methods, additional references, Nature Research reporting summaries, source data, extended data, supplementary information, acknowledgements, peer review information; details of author contributions and competing interests; and statements of data and code availability are available at <https://doi.org/10.1038/s41586-020-2716-8>.

- Mühlbauer, S. et al. Skyrmion lattice in a chiral magnet. *Science* **323**, 915–919 (2009).
- Yu, X. Z. et al. Real-space observation of a two-dimensional skyrmion crystal. *Nature* **465**, 901–904 (2010).
- Nagaosa, N. & Tokura, Y. Topological properties and dynamics of magnetic skyrmions. *Nat. Nanotechnol.* **8**, 899–911 (2013).
- Fert, A., Reyren, N. & Cros, V. Magnetic skyrmions: advances in physics and potential applications. *Nat. Rev. Mater.* **2**, 17031 (2017).
- Baltz, V. et al. Antiferromagnetic spintronics. *Rev. Mod. Phys.* **90**, 015005 (2018).
- Barker, J. & Tretiakov, O. A. Static and dynamical properties of antiferromagnetic skyrmions in the presence of applied current and temperature. *Phys. Rev. Lett.* **116**, 147203 (2016).
- Zhang, X., Zhou, Y. & Ezawa, M. Antiferromagnetic skyrmion: stability, creation and manipulation. *Sci. Rep.* **6**, 24795 (2016).
- Rosales, H. D., Cabra, D. C. & Pujol, P. Three-sublattice skyrmion crystal in the antiferromagnetic triangular lattice. *Phys. Rev. B* **92**, 214439 (2015).
- Díaz, S. A., Klinovaja, J. & Loss, D. Topological magnons and edge states in antiferromagnetic skyrmion crystals. *Phys. Rev. Lett.* **122**, 187203 (2019).
- Kamiya, Y. & Batista, C. D. Magnetic vortex crystals in frustrated Mott insulator. *Phys. Rev. X* **4**, 011023 (2014).

- Lin, S.-Z., Saxena, A. & Batista, C. D. Skyrmion fractionalization and merons in chiral magnets with easy-plane anisotropy. *Phys. Rev. B* **91**, 224407 (2015).
- Yu, X. Z. et al. Transformation between meron and skyrmion topological spin textures in a chiral magnet. *Nature* **564**, 95–98 (2018).
- Wen, X.-G. Zoo of quantum-topological phases of matter. *Rev. Mod. Phys.* **89**, 041004 (2017).
- Jonietz, F. et al. Spin transfer torques in MnSi at ultralow current densities. *Science* **330**, 1648–1651 (2010).
- Yu, X. et al. Skyrmion on near room temperature in an ultralow current density. *Nat. Commun.* **3**, 988 (2012).
- White, J. S. et al. Electric field control of the skyrmion lattice in Cu_2OSeO_3 . *J. Phys. Condens. Matter* **24**, 432201 (2012).
- Rößler, U. K., Bogdanov, A. N. & Peiderer, C. Spontaneous skyrmion ground states in magnetic metals. *Nature* **442**, 797–801 (2006).
- Kurumaji, T. et al. Skyrmion lattice with a giant topological Hall effect in a frustrated triangular-lattice magnet. *Science* **365**, 914–918 (2019).
- Hirschberger, M. et al. Skyrmion phase and competing magnetic orders on a breathing kagomé lattice. *Nat. Commun.* **10**, 5831 (2019).
- Khanh, N. D. et al. Nanometric square skyrmion lattice in a centrosymmetric tetragonal magnet. *Nat. Nanotechnol.* **15**, 444–449 (2020).
- Sokolov, D. A. et al. Metamagnetic texture in a polar antiferromagnet. *Nat. Phys.* **15**, 671–677 (2019).
- Balents, L. Spin liquids in frustrated magnets. *Nature* **464**, 199–208 (2010).
- Okubo, T., Chung, S. & Kawamura, H. Multiple- \mathbf{q} states and the skyrmion lattice of the triangular-lattice Heisenberg antiferromagnet under magnetic fields. *Phys. Rev. Lett.* **108**, 017206 (2012).
- Leonov, A. O. & Mostovoy, M. Multiply periodic states and isolated skyrmions in an anisotropic frustrated magnet. *Nat. Commun.* **6**, 8275 (2015).
- Sutcliffe, P. Skyrmion knots in frustrated magnets. *Phys. Rev. Lett.* **118**, 247203 (2017).
- Rybakov, F. N. et al. Magnetic hopfions in solids. Preprint at <https://arxiv.org/abs/1904.00250> (2019).
- Lohani, V., Hickey, C., Masell, J. & Rosch, A. Quantum skyrmions in frustrated ferromagnets. *Phys. Rev. X* **9**, 041063 (2019).
- Fritsch, V. et al. Spin and orbital frustration in MnSc_2S_4 and FeSc_2S_4 . *Phys. Rev. Lett.* **92**, 116401 (2004).
- Gao, S. et al. Spiral spin-liquid and the emergence of a vortex-like state in MnSc_2S_4 . *Nat. Phys.* **13**, 157–161 (2017).
- Bergman, D., Alicea, J., Gull, E., Trebst, S. & Balents, L. Order-by-disorder and spiral spin liquid in frustrated diamond-lattice antiferromagnets. *Nat. Phys.* **3**, 487–491 (2007).
- Lee, S. & Balents, L. Theory of the ordered phase in A-site antiferromagnetic spinels. *Phys. Rev. B* **78**, 144417 (2008).
- Iqbal, Y., Müller, T., Jeschke, H. O., Thomale, R. & Reuther, J. Stability of the spiral spin liquid in MnSc_2S_4 . *Phys. Rev. B* **98**, 064427 (2018).
- Zharko, N. O. et al. Spin liquid in a single crystal of the frustrated diamond lattice antiferromagnet CoAl_2O_4 . *Phys. Rev. B* **84**, 094403 (2011).
- MacDougall, G. J. et al. Revisiting the ground state of CoAl_2O_4 : comparison to the conventional antiferromagnet MnAl_2O_4 . *Phys. Rev. B* **94**, 184422 (2016).
- Ge, L. et al. Spin order and dynamics in the diamond-lattice Heisenberg antiferromagnets CuRh_2O_4 and CoRh_2O_4 . *Phys. Rev. B* **96**, 064413 (2017).
- Watanabe, H. On the ground level splitting of Mn^{2+} and Fe^{3+} in nearly cubic crystalline field. *Prog. Theor. Phys.* **18**, 405–420 (1957).
- Akagi, Y., Udagawa, M. & Motome, Y. Hidden multiple-spin interactions as an origin of spin scalar chiral order in frustrated Kondo lattice models. *Phys. Rev. Lett.* **108**, 096401 (2012).
- Hayami, S., Ozawa, R. & Motome, Y. Effective bilinear–biquadratic model for noncoplanar ordering in itinerant magnets. *Phys. Rev. B* **95**, 224424 (2017).
- Milde, P. et al. Unwinding of a skyrmion lattice by magnetic monopoles. *Science* **340**, 1076–1080 (2013).
- Karube, K. et al. Robust metastable skyrmions and their triangular-square lattice structural transition in a high-temperature chiral magnet. *Nat. Mater.* **15**, 1237–1242 (2016).
- Attig, J. & Trebst, S. Classical spin spirals in frustrated magnets from free-fermion band topology. *Phys. Rev. B* **96**, 085145 (2017).
- Balla, P., Iqbal, Y. & Penc, K. Affine lattice construction of spiral surfaces in frustrated Heisenberg models. *Phys. Rev. B* **100**, 140402 (2019).
- Göbel, B., Mook, A., Henk, J. & Mertig, I. Antiferromagnetic skyrmion crystals: generation, topological Hall, and topological spin Hall effect. *Phys. Rev. B* **96**, 060406 (2017).
- Bessarab, P. F. et al. Stability and lifetime of antiferromagnetic skyrmions. *Phys. Rev. B* **99**, 140411 (2019).
- van Hoogdalem, K. A., Tserkovnyak, Y. & Loss, D. Magnetic texture-induced thermal Hall effects. *Phys. Rev. B* **87**, 024402 (2013).
- Daniels, M. W., Yu, W., Cheng, R., Xiao, J. & Xiao, D. Topological spin Hall effects and tunable skyrmion Hall effects in uniaxial antiferromagnetic insulators. *Phys. Rev. B* **99**, 224433 (2019).
- Roldán-Molina, A., Nunez, A. S. & Fernández-Rossier, J. Topological spin waves in the atomic-scale magnetic skyrmion crystal. *New J. Phys.* **18**, 045015 (2016).

Publisher's note Springer Nature remains neutral with regard to jurisdictional claims in published maps and institutional affiliations.

© The Author(s), under exclusive licence to Springer Nature Limited 2020

Inelastic neutron scattering experiments

INS experiments on a powder sample of MnSc_2S_4 were performed on the FOCUS time-of-flight spectrometer at the Swiss Spallation Neutron Source (SINQ) of Paul Scherrer Institut (PSI). For the measurements, about 4 g of MnSc_2S_4 powder sample synthesized through solid-state reactions⁴⁸ was placed into an annular-shaped aluminium can with outer and inner diameters of 12 mm and 10 mm, respectively. An Orange cryostat with an additional roots pump was used, enabling a base temperature of 1.3 K. The incoming neutron wavelength was 5.0 Å.

INS experiments on a single-crystal sample of MnSc_2S_4 grown with the chemical transport reaction technique²⁹ were performed on the cold-neutron three-axis spectrometer ThALES^{49,50} at Institut Laue-Langevin (ILL) and the cold-neutron three-axis spectrometer PANDA^{51,52} at Heinz Maier-Leibnitz Zentrum (MLZ). Five crystals with a total mass of ~100 mg were co-aligned with $(hk0)$ as the horizontal scattering plane. For the experiment on ThALES, a cryomagnet and an additional roots pump were used, which enabled a base temperature of 1.2 K and a maximal vertical field of 10 T. For better resolution, the Si(111) monochromator and PG(002) analyser with double focusing were used. A Be filter was mounted between the sample and analyser and a radial collimator was installed between the analyser and the detector. The final neutron momentum k_f was fixed at 1.3 Å⁻¹. For the experiment on PANDA, a ³He cryostat was used, which enabled a base temperature of ~0.5 K. The PG(002) monochromator and analyser with double focusing were employed. The final neutron momentum k_f was fixed at 1.3 Å⁻¹. A cooled Be filter was mounted before the sample to remove the higher-order neutrons.

Linear spin-wave calculations and fits for the INS spectra were performed using the SpinW package⁵³. The input data for the fits were the three integrated intensities $I(\omega)$ shown in Fig. 1b. The spin Hamiltonian of the J_1 - J_2 - J_3 model has the helical ground state with propagation vector $\mathbf{q} = (0.75, 0.75, 0)$.

Neutron diffraction experiments

The neutron diffraction experiment was performed on the diffractometer D23 at ILL to map out the phase diagram shown in Fig. 3. An incoming neutron wavelength of 1.27 Å was selected by the Cu(200) monochromator. A dilution refrigerator with a base temperature of 50 mK and a magnet that supplied fields up to 12 T were employed. The MnSc_2S_4 crystal was aligned with the (111) direction along the vertical field direction. To map out the phase diagram, we first cooled the crystal in zero field and then performed a rocking scan for the $(0.75, -0.75, 0)$ reflection with increasing and decreasing fields.

The neutron diffraction dataset in the triple- \mathbf{q} phase was collected on the TriCS (now ZEBRA) single-crystal diffractometer at SINQ, PSI. An incoming neutron wavelength of 2.32 Å was selected by the PG(002) monochromator. A PG filter was mounted before the sample. A cryomagnet and a roots pump were employed for the measurements. 67 reflections were collected at $T = 1.60$ K in a magnetic field of 3.5 T along the [111] direction.

Monte Carlo simulations

Monte Carlo simulations were performed using the Metropolis algorithm by lowering the temperature in an annealing scheme and computing 500 independent runs initialized by different random numbers for each temperature and external magnetic field. Simulations were performed in $2 \times L^3$ magnetic site clusters, with $L = 8$ –24 and periodic boundary conditions. To compare the classical Monte Carlo simulations with the experimental results, the S^2 factor in the computed thermal averages of the relevant quantities was replaced by the quantum mechanical expectation value $\langle S \rangle^2 = S(S+1)$ following ref.⁵⁴.

Comparison for different spin models

Using linear spin-wave theory, we compared different spin models against the INS spectra collected on a powder sample of MnSc_2S_4 . Extended Data Fig. 1a, b shows the experimental data and the spin-wave calculation results for the J_1 - J_2 - J_3 model with $J_1 = -0.31$ K, $J_2 = 0.46$ K and $J_3 = 0.087$ K, respectively. For the J_1 - J_2 model with $J_3 = 0$, if the spectra at $Q \approx 0.4$ Å are fitted to the experimental data, the calculated INS intensity reaches ~1.2 meV at $Q \approx 0.9$ Å, as shown in Extended Data Fig. 1c, which is higher than the experimental bandwidth of ~0.9 meV. Therefore, the third-neighbour coupling J_3 is necessary to achieve a good fit for the INS spectra. The ratio J_2/J_1 is now increased to ~1.5, compared to 0.85 from neutron diffuse scattering²⁹, indicating that the lattice is more frustrated than anticipated. As shown in Extended Data Fig. 2, at temperatures above T_N , the J_1 - J_2 - J_3 model leads to stronger intensities at around $\mathbf{q} = (0.75, 0.75, 0)$, which reproduces the intensity contrast within the spiral surface that was observed in our previous experiment²⁹.

Recent density functional theory (DFT) calculations³² suggest a different J_1 - J_2 - J_3 model with $J_1 = -0.378$ K, $J_2 = 0.621$ K and $J_3 = 0.217$ K. From the calculated INS spectra shown in Extended Data Fig. 1d, we see that this DFT model produces a magnon bandwidth that is higher than the experimental observation. Compared to the coupling strengths fitted from the spin-wave dispersions, the DFT model overestimates the coupling strength for J_2 and J_3 .

Theoretical phase diagram from the Monte Carlo simulations

Extended Data Fig. 3 shows the calculated phase diagram obtained from Monte Carlo simulations using the perturbed spin Hamiltonian (equation (1)). The J_1, J_2 and J_3 couplings are fixed to the spin-wave fits of the INS spectra, whereas the anisotropy terms are determined to be $J_{||} = -0.01$ K and $A_4 = 0.0016$ K after exploring the stability of the triple- \mathbf{q} phase as discussed below. The colour scale denotes the absolute value of the total scalar spin chirality $\chi_{\text{tot}} = \left\langle \frac{1}{8\pi} \sum_n \chi_n \right\rangle$ with $\chi_n = \mathbf{S}_i \cdot (\mathbf{S}_j \times \mathbf{S}_k)$, where n indexes the N elementary triangles of sites i, j and k in the (111) layers.

In zero magnetic field the single- \mathbf{q} helical state is identified by $\chi = 0$. The transient collinear and incommensurate phases found experimentally in the vicinity of T_N (ref.²⁹) are not reproduced in our simulations, possibly owing to thermal fluctuations and finite-size effects, and a detailed exploration in the transitional regime is deferred for future analysis. In the applied magnetic fields the triple- \mathbf{q} phase is identified by a sharp increase of the total scalar spin chirality, which evidences a magnetic structure that is topologically different from the single- \mathbf{q} helical phase. In contrast to the skyrmion lattice, which is stabilized by antisymmetric Dzyaloshinskii–Moriya interactions⁵, here the winding direction can be either clockwise or counter-clockwise because the model preserves the inversion symmetry in the (111) plane²³. This implies a spontaneous symmetry breaking in the antiferromagnetic skyrmion lattice phase.

Two complementary methods were used to clarify the antiferromagnetic skyrmion lattice state using Monte Carlo simulations. One is to directly check the magnetic textures in real space, as exemplified in Fig. 4, and the other is to calculate the magnetic structure factors in reciprocal space, which can be directly compared to the neutron diffraction results. In the latter method, the skyrmion phase can be identified by the six Bragg spots located in the plane perpendicular to the magnetic field. Extended Data Fig. 4 shows the calculated magnetic structure factors in the $(hk0)$ and (111) planes at $T = 1.25$ K and $B_{||} = 5.6$ T using a $16 \times 16 \times 16$ super-lattice over 500 averaged copies.

To illustrate the stability of the triple- \mathbf{q} phase and explain how we determined the strength of the perturbation terms, we compare phase diagrams calculated with different strengths of $J_{||}$ in Extended Data Fig. 5. When the strength of $J_{||}$ is reduced from ~0.01 K to ~0.005 K, the stability region of the triple- \mathbf{q} phase will also be reduced and thus deviate from our experimental observation. On the other hand, when the

strength of J_{\parallel} is increased to -0.02 K, although the stability region of the triple- \mathbf{q} phase remains almost the same, a new chiral phase emerges at lower magnetic fields, which is possibly a multiple- \mathbf{q} state that is different from the skyrmion, fractional skyrmion and meron lattices. Finally, when the sign of J_{\parallel} becomes positive with $J_{\parallel} = 0.01$ K, the triple- \mathbf{q} phase will disappear completely. Therefore, the perturbation term J_{\parallel} is determined to be -0.01 K.

Analytical expression for the antiferromagnetic skyrmion lattice

As confirmed in many types of skyrmion lattice, the magnetic structure of each \mathbf{q} component of the triple- \mathbf{q} structure is often related to the single- \mathbf{q} structure observed in zero field. A well known example is the Bloch-type skyrmion lattice in MnSi (ref. ¹), where the helical components are derived from the zero-field helical phase. Similar arguments hold for the cycloidal components of the Néel-type skyrmion lattice observed in GaV₄S₈ (ref. ⁵⁵). Therefore, considering the helical and collinear structures that are observed in MnSc₂S₄ at zero field, we can express its field-induced triple- \mathbf{q} structure through the ansatz:

$$\mathbf{S}(\mathbf{r}) = \frac{1}{n_S} \left[A_{\perp} \sum_{i=1}^3 \sin(\mathbf{q}_i \cdot \mathbf{r} + \phi_{\perp}) \hat{\mathbf{e}}_i + A_{\parallel} \sum_{i=1}^3 \cos(\mathbf{q}_i \cdot \mathbf{r} + \phi_{\parallel}) \hat{\mathbf{e}}_{\parallel} + \mathbf{M}_{\parallel} \right], \quad (2)$$

where n_S is the normalization factor that fixes the spin magnitude to $5/2$, A_{\perp} (A_{\parallel}) is the amplitude for spin modulation perpendicular (parallel) to the [111] direction $\hat{\mathbf{e}}_{\parallel}$ with phase factor $\phi_{\perp,i} = \phi_{\perp}$ ($\phi_{\parallel,i} = \phi_{\parallel}$), \mathbf{q}_i are the three propagation vectors $(0.75, -0.75, 0)$, $(0.75, 0, -0.75)$ and $(0, 0.75, -0.75)$, $\hat{\mathbf{e}}_i$ are the unitary vectors that form Cartesian coordinate systems with the corresponding \mathbf{q}_i and $\hat{\mathbf{e}}_{\parallel}$, and \mathbf{M}_{\parallel} is a homogeneous contribution to the magnetization along $\hat{\mathbf{e}}_{\parallel}$.

Assuming equal magnitude for A_{\perp} and A_{\parallel} , and $\phi_{\perp} = 0$, without loss of generality, the case of $\phi_{\parallel} = -\pi$ and $-3\pi/2$ corresponds to helical and collinear components, respectively (see Extended Data Fig. 6a). We note that for the zero-field collinear structure, the spin directions are canted out of the (111) plane by 45° according to our previous refinement²⁹, and such a canting has been taken into account in our expression. Therefore, by varying ϕ_{\parallel} , we can construct different triple- \mathbf{q} structures with \mathbf{q} components covering the observed collinear structure, helical structure and, most importantly, a general distorted structure that lies between the collinear and helical phases.

Extended Data Fig. 6b shows the representative magnetic structure of the proposed ansatz for one sublattice in the (111) plane together with that obtained from the Monte Carlo simulations. Assuming $|\mathbf{M}_{\parallel}| = 1$ and the parameter set of $A_{\parallel} = -A_{\perp} = 2.2$, $\phi_{\perp} = 0$ and $\phi_{\parallel} = -9\pi/8$, the proposed ansatz reproduces well the magnetic structure obtained in the Monte Carlo simulations. Two very important details can be observed in this result. First, unlike the typical skyrmion lattice, the internal phase for the spin configuration is different for the perpendicular and parallel components of the spin, $\phi_{\perp,i} \neq \phi_{\parallel,i}$. Second, the condition $\sum_i \cos \phi_i = 1$ is not satisfied as usual in triple- \mathbf{q} phases²³.

Refinement of the neutron diffraction dataset in the triple- \mathbf{q} phase

With the ansatz presented in the previous section, we can directly verify the antiferromagnetic skyrmion lattice by comparing its magnetic structure factors with the neutron diffraction intensities of magnetic Bragg peaks. As shown in Extended Data Fig. 7a, the fractional antiferromagnetic skyrmion lattice obtained in the Monte Carlo simulation fits the neutron diffraction dataset very well, with $R_{F2} = 14.3\%$ and $R_f = 10.8\%$.

By varying the ϕ_{\parallel} phase factors, we compared the refinement results from different triple- \mathbf{q} structures that are composed of general distorted helical components. Extended Data Fig. 7b summarizes the

dependence of R_{F2} on ϕ_{\parallel} . The best refinement was achieved in the region $-9\pi/8 \leq \phi_{\parallel} \leq -7\pi/8$ with comparable R -factors, justifying the value of $\phi_{\parallel} = -9\pi/8$ obtained from the Monte Carlo simulations. More importantly, as shown in Extended Data Fig. 7c, in the entire regime of $-9\pi/8 \leq \phi_{\parallel} \leq -7\pi/8$, the triple- \mathbf{q} structure can always be described as a fractional antiferromagnetic skyrmion lattice, that is, each (111) plane exhibits a three-sublattice antiferromagnetic alignment and a fractional skyrmion lattice emerges in each sublattice. The only difference in these structures is a slight variation in the fractionalization. Therefore, our neutron diffraction results strongly support the emergence of a fractional three-sublattice antiferromagnetic skyrmion lattice in MnSc₂S₄.

Data availability

The data that support the findings of this study are available at <https://doi.org/10.5281/zenodo.3902757> and from the corresponding author upon reasonable request.

Code availability

The codes for the spin-wave calculations and the Monte Carlo simulations that support the findings of this study are available from the corresponding author upon reasonable request.

48. Krimmel, A. et al. Magnetic ordering and spin excitations in the frustrated magnet MnSc₂S₄. *Phys. Rev. B* **73**, 014413 (2006).
49. Boehm, M. et al. ThALES—three axis low energy spectroscopy for highly correlated electron systems. *Neutron News* **26**, 18–21 (2015).
50. Zaharko, O. et al. Spin dynamics in the order-by-disorder candidate MnSc₂S₄. Report <https://doi.org/10.5291/ILL-DATA.4-01-1500> (Institut Laue-Langevin, 2016).
51. Schneidewind, A. & Čermák, P. PANDA: cold three axes spectrometer. *J. Large-Scale Res. Facilities* **1**, A12 (2015).
52. Utschick, C., Skoulatos, M., Schneidewind, A. & Böni, P. Optimizing the triple-axis spectrometer PANDA at the MLZ for small samples and complex sample environment conditions. *Nucl. Instr. Meth. Phys. Res. A* **837**, 88–91 (2016).
53. Toth, S. & Lake, B. Linear spin wave theory for single-Q incommensurate magnetic structures. *J. Phys. Condens. Matter* **27**, 166002 (2015).
54. Johnston, D. C. et al. Magnetic exchange interactions in BaMn₂As₂: a case study of the J_1 - J_2 - J_c Heisenberg model. *Phys. Rev. B* **84**, 094445 (2011).
55. Kézsmárki, I. et al. Néel type skyrmion lattice with confined orientation in the polar magnetic semiconductor GaV₄S₈. *Nat. Mater.* **14**, 1116–1122 (2015).

Acknowledgements We acknowledge S. Tóth and S. Ward for help in the analysis of the neutron spectra. We thank A. Scaramucci for the initial trial of the Monte Carlo simulations. We acknowledge discussions with M. Pregelj, S. B. Lee, T.-h. Arima, T. Nakajima, J. S. White and Y. Su. S.G. acknowledges discussions at RIKEN CEMS. F.A.G.A. and H.D.R. thank R. Borzi for discussions. H.D.R. thanks M. Zhitomirsky for discussions about the Monte Carlo simulations. Our neutron scattering experiments were performed at the SINQ, PSI, Villigen, Switzerland, at MLZ, Garching, Germany and at ILL, Grenoble, France. This work was supported by the Swiss National Science Foundation under grant numbers 20021-140862 and 20020-152734, by the SCOPES project number IZ73Z0-152734/1 and by Centro Latinoamericano-Suizo under the Seed money grant number SMG1811. Our work was additionally supported by Deutsche Forschungsgemeinschaft of the Transregional Collaborative Research Center TRR 80. D.C.C., F.A.G.A. and H.D.R. are partially supported by CONICET (PIP 2015-813), SECyT UNLP P+D X792 and X788, PPIID X039. H.D.R. acknowledges support from PICT 2016-4083.

Author contributions O.Z. designed and coordinated the project. V.T. prepared the single crystals. S.G., O.Z. and C.R. performed the INS experiments with T.F. as the local contact for FOCUS, P.S. and M.B. for ThALES and P.C. and A.S. for PANDA. S.G. analysed the neutron spectra with input from O.Z., T.F. and C.R. Neutron diffraction experiments were performed by G.K. and O.Z. with E.R. as the local contact. Theoretical analysis and Monte Carlo simulations were performed by H.D.R., F.A.G.A. and D.C.C. The manuscript was prepared by S.G., H.D.R. and O.Z. with input from all co-authors.

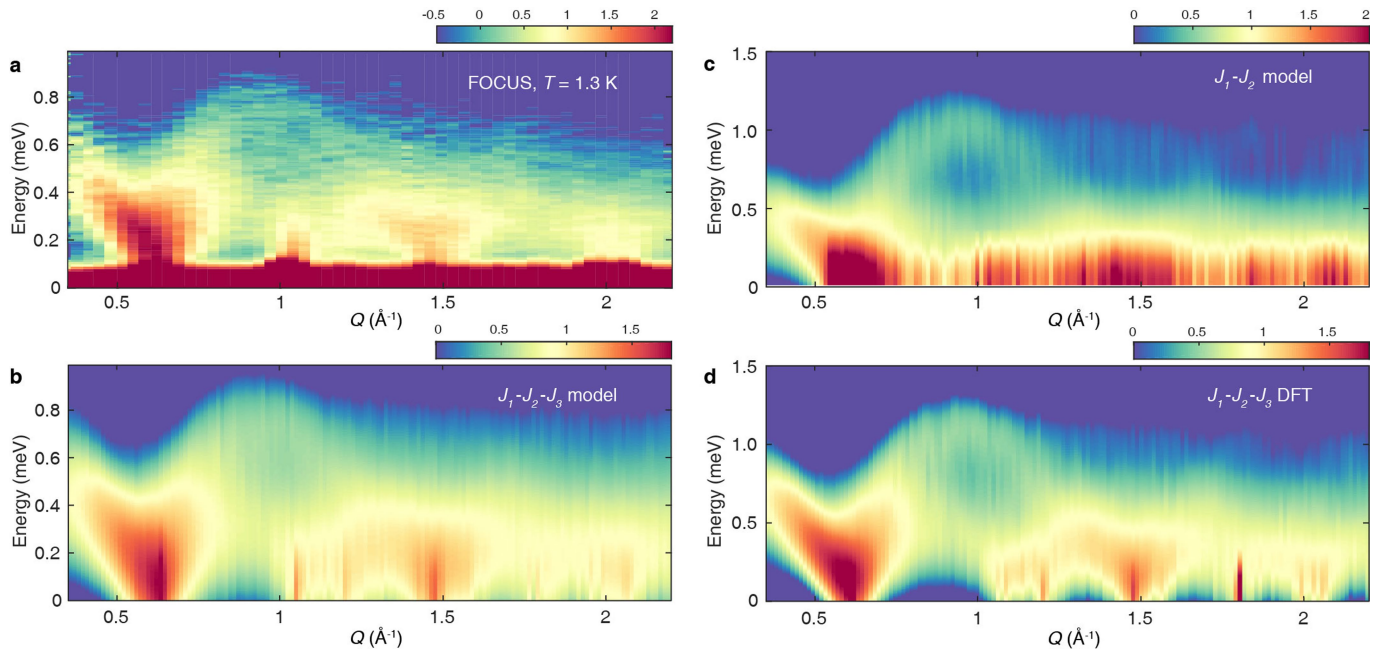
Competing interests The authors declare no competing interests.

Additional information

Correspondence and requests for materials should be addressed to O.Z.

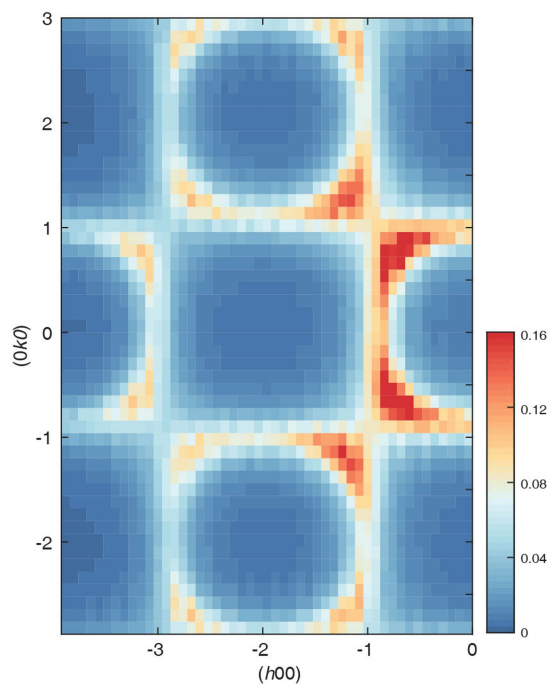
Peer review information *Nature* thanks Yoshitomo Kamiyura and the other, anonymous, reviewer(s) for their contribution to the peer review of this work.

Reprints and permissions information is available at <http://www.nature.com/reprints>.



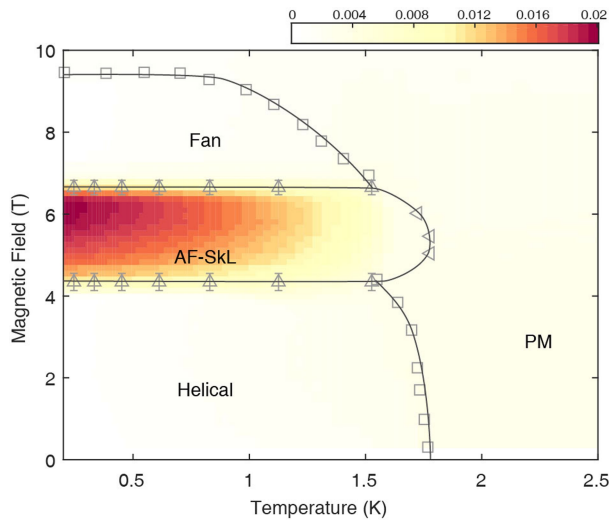
Extended Data Fig. 1 | Comparison of different spin models. **a**, INS spectra $S(Q, \omega)$ collected on FOCUS at $T = 1.3$ K using a powder sample of MnSc_2S_4 . **b-d**, INS spectra calculated using the linear spin-wave theory for the J_1 - J_2 - J_3 model with $J_1 = -0.31$ K, $J_2 = 0.46$ K and $J_3 = 0.087$ K, as discussed in the main text

(**b**), for the J_1 - J_2 model with $J_1 = -0.71$ K, $J_2 = -0.85 \times J_1 = 0.60$ K (**c**), and for the J_1 - J_2 - J_3 model with parameters calculated from the DFT calculations³², $J_1 = -0.378$ K, $J_2 = 0.621$ K and $J_3 = 0.217$ K. Note the different energy ranges in different panels.



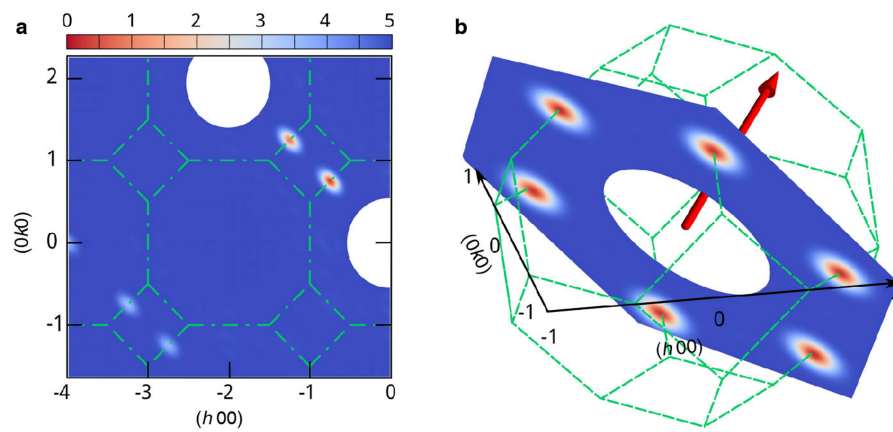
Extended Data Fig. 2 | Spiral surface above the long-range order transition.

Spin correlations in the $(hk0)$ plane calculated by Monte Carlo simulations using the J_1 - J_2 - J_3 model and the anisotropic perturbation terms with coupling strength listed in the main text. Calculations were performed at $T = 2.9$ K. Calculations with zero anisotropic perturbations do not affect the results.

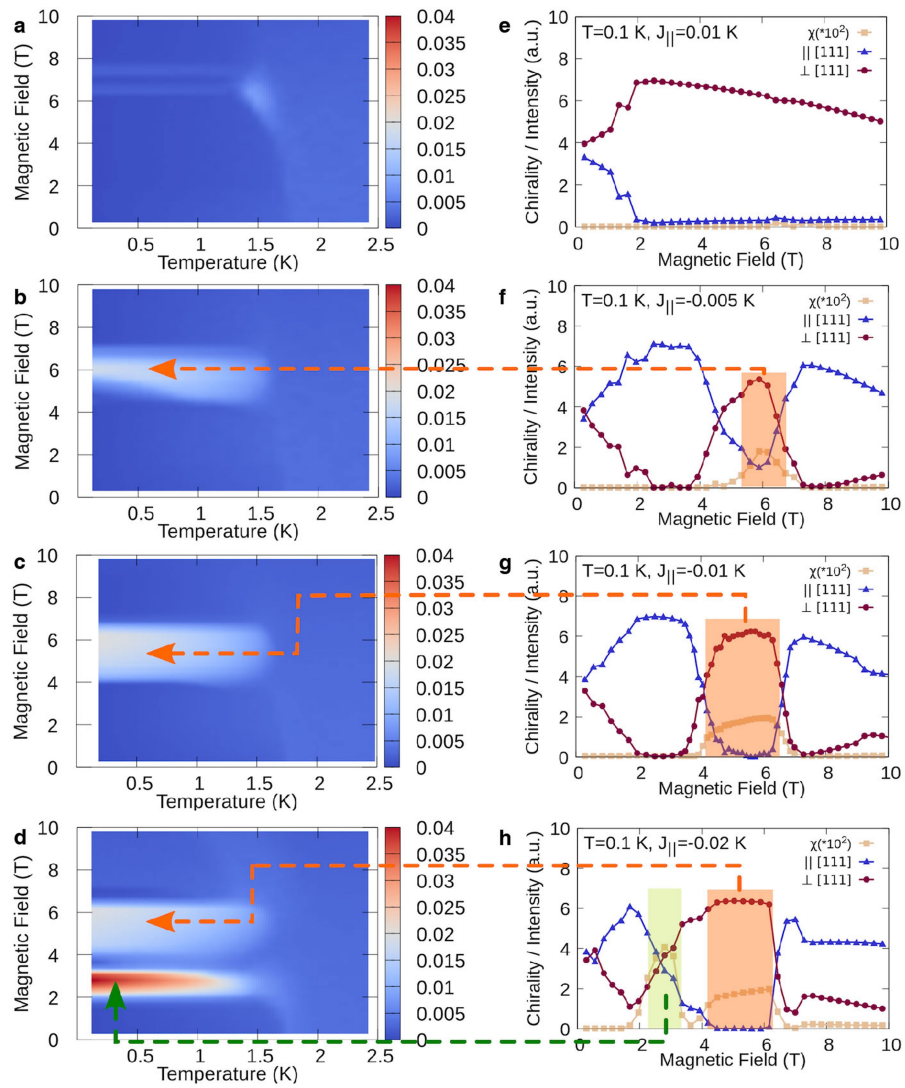


Extended Data Fig. 3 | Calculated phase diagram with perturbations

$J_{\parallel} = -0.01 \text{ K}$ and $A_4 = 0.0016 \text{ K}$. Phase diagram for MnSc₂S₄ obtained from Monte Carlo simulations with a field applied along the [111] direction as in the experiment. The colour map shows the calculated absolute value of the total scalar spin chirality, χ_{tot} . Squares indicate the phase boundary obtained from the peak position of the calculated magnetic susceptibility in field along the [111] direction. Up-pointing triangles on the boundary of the antiferromagnetic skyrmion lattice (AF-SkL) phase are the middle points of the steep rise/drop in χ_{tot} as a function of magnetic field at constant T , and their errors are estimated using the half-width of the transitional region. Left-pointing triangles mark the sudden rise in $\chi_{\text{tot}}(T)$ in constant field. Error bars representing the standard deviations are not shown if their length is smaller than the marker size.

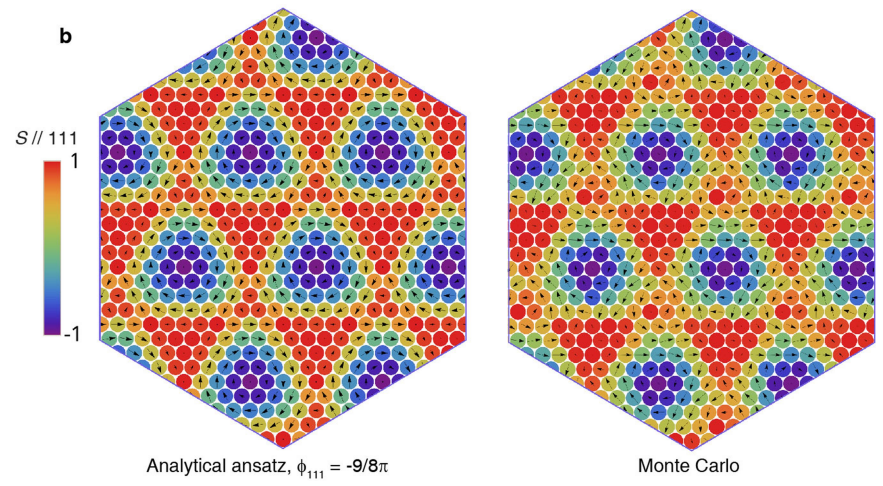
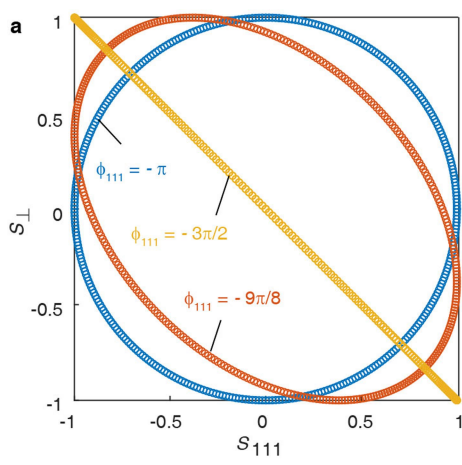


Extended Data Fig. 4 | Identifying the triple- q phase. Magnetic structure factor obtained by simulations in the triple- q phase at $T=1.25$ K and $B_{111}=5.6$ T in the $(hk0)$ (a) and (111) (b) planes.



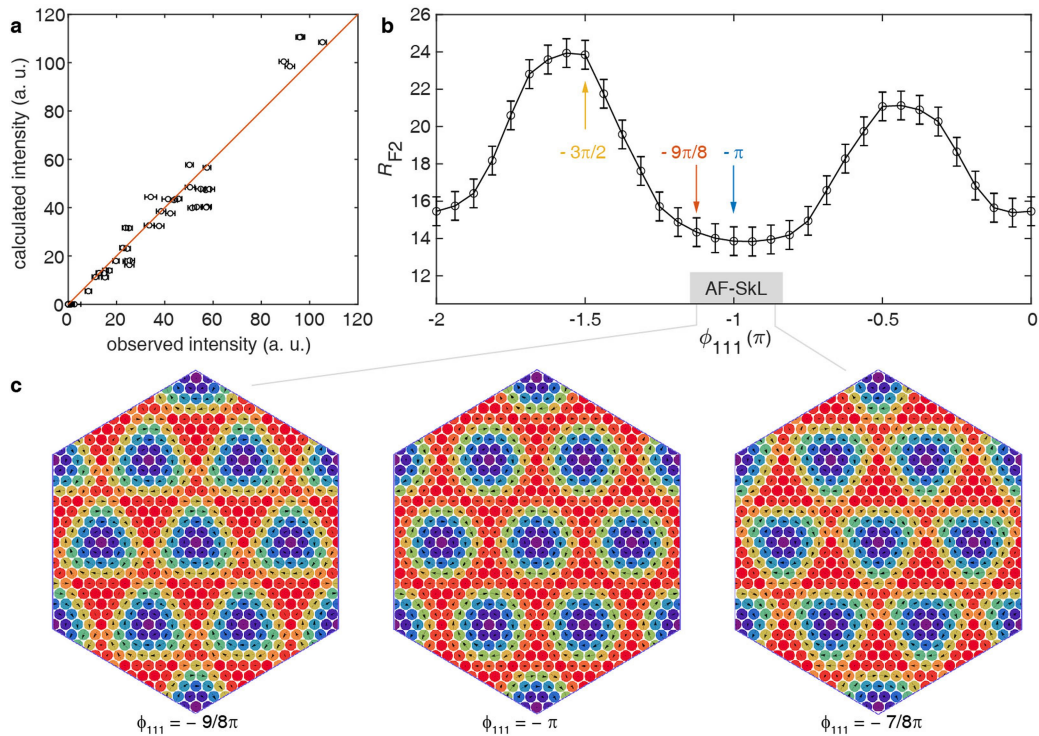
Extended Data Fig. 5 | Dependence of the triple- q phase stability on the perturbation terms $J_{||}$. **a-d**, Calculated phase diagrams with perturbations $J_{||} = 0.01$ K (**a**), -0.005 K (**b**), -0.01 K (**c**) and -0.02 K (**d**). The single-ion anisotropy A_4 is fixed at 0.0016 K. The colour map shows the absolute value of the total scalar spin chirality as in Extended Data Fig. 3. **e-h**, Field dependence

of the domain population at $T = 0.1$ K. Red circles and blue triangles indicate domains with q in and out of the (111) plane, respectively. Yellow squares are the calculated absolute values of the scalar spin chirality. Error bars representing the standard deviations of the mean are smaller than the marker size.



Extended Data Fig. 6 | Analytical ansatz for the antiferromagnetic skyrmion lattice. **a**, Schematic for the moment directions in each \mathbf{q} component of the triple- \mathbf{q} structure at $\phi_{111} = -\pi$ (helical), $-3\pi/2$ (collinear) and $-9\pi/8$ (distorted helical). **b**, Comparison between the representative magnetic

texture for one sublattice in the (111) plane obtained by the analytical ansatz (left) and Monte Carlo simulations (right) performed at $T = 0.5$ K and $B_{111} = 5$ T. The colour scheme indicates the spin component along the [111] direction, and the arrows show the spin component in the (111) plane.



Extended Data Fig. 7 | Refinement of the neutron diffraction dataset collected in the triple- \mathbf{q} phase. **a**, Comparison of observed and calculated intensities for the fractional antiferromagnetic skyrmion lattice. The dataset was collected in the triple- \mathbf{q} phase under a magnetic field of 3.5 T along the [111] direction. **b**, Dependence of the R_{F2} factor on the phase factor ϕ_{111} . The arrows indicate results for $\phi_{111} = -\pi$, $-3\pi/2$ and $-9\pi/8$, which correspond to the triple- \mathbf{q} structures with helical, collinear and distorted helical components, respectively. The error bars correspond to the standard deviations of the

measured neutron intensities (**a**) and the refined phase factor (**b**). **c**, Magnetic textures for one sublattice in the (111) plane with $\phi_{111} = -9\pi/8$, $-\pi$ and $-7\pi/8$, showing that in the region $-9\pi/8 \leq \phi_{111} \leq -7\pi/8$ the triple- \mathbf{q} structure always realizes a fractional antiferromagnetic skyrmion lattice, and only the proportion of fractionalization is varied. The colour scheme indicates the spin component along the [111] direction, and the arrows show the spin component in the (111) plane.